Journal of Zhejiang University-SCIENCE C (Computers & Electronics)
ISSN 1869-1951 (Print); ISSN 1869-196X (Online)
www.zju.edu.cn/jzus; www.springerlink.com
E-mail: jzus@zju.edu.cn

Three-dimensional organ modeling based on deformable surfaces applied to radio-oncology*

Gloria BUENO†[1], Oscar DÉNIZ[1], Jesús SALIDO[1], Carmen CARRASCOSA[2], José M. DELGADO[3]

([1]*Grupo de Visión y Sistemas Inteligentes, Universidad de Castilla-La Mancha, E.T.S. Ingenieros Industriales Avda. Camilo José Cela, 3. 13071 Ciudad Real, Spain*)

([2]*Hospital General de Ciudad Real, Tomelloso s/n. 13005 Ciudad Real, Spain*)

([3]*Instituto Oncológico (Grupo IMO) Modesto Lafuente, 14, 28010 Madrid, Spain*)

†E-mail: Gloria.Bueno@uclm.es

Received July 4, 2009; Revision accepted Apr. 1, 2010; Crosschecked May 4, 2010

Abstract: This paper describes a method based on an energy minimizing deformable model applied to the 3D biomechanical modeling of a set of organs considered as regions of interest (ROI) for radiotherapy. The initial model consists of a quadratic surface that is deformed to the exact contour of the ROI by means of the physical properties of a mass-spring system. The exact contour of each ROI is first obtained using a geodesic active contour model. The ROI is then parameterized by the vibration modes resulting from the deformation process. Once each structure has been defined, the method provides a 3D global model including the whole set of ROIs. This model allows one to describe statistically the most significant variations among its structures. Statistical ROI variations among a set of patients or through time can be analyzed. Experimental results are presented using the pelvic zone to simulate anatomical variations among structures and its application in radiotherapy treatment planning.

Key words: 3D biomechanical organ modeling, Energy minimizing deformable model, Finite element model, Geodesic active contour, Radiotherapy treatment planning

doi:10.1631/jzus.C0910402 **Document code:** A **CLC number:** TP391.4; R73

1 Introduction

Three-dimensional (3D) organ modeling is of key importance to improve the conformation of the dose delivered to the target (tumoral tissues), whatever its shape, in order to spare surrounding tissues. Here the term 'modeling' refers to the biomechanical modeling of organs, and how it can be used to describe organ movements, and therefore to guide segmentation and registration when the organs have deformed. Thus, 3D organ modeling may be applied for several purposes including segmentation, registration, and tracking (Foskey *et al.*, 2005; Webb, 2006). An essential part of the conformal treatment planning procedure is the segmentation of target volumes and organs at risk in computerized tomography (CT) images (Costa *et al.*, 2007). Because of the difficulty of accurately and reliably delineating structures in medical images, this work has been typically done manually by radiation oncologists (Lee and Chung, 2004; Banik *et al.*, 2009). However, manual delineation is tedious, time consuming, and also prone to errors due to intra- and inter-user variability (Collier *et al.*, 2003; Costa *et al.*, 2007).

Moreover, recent advances in intensity modulated radiotherapy treatment (IMRT) call for a greater understanding of uncertainties in the treatment process and more rigorous protocols leading to greater precision in treatment delivery. The

* Project partially supported by the VI FP and VII FP of the European Commission through MAESTRO and ENVISION projects (Nos. IP CE503564 and SP CE241851) and Spanish Junta de Comunidades de Castilla–La Mancha (Nos. PBC06-0019 and PI-2006/01.1)

treatment of organs comprised of soft tissue and those subject to rhythmic movements cause inter- and intra-fraction motion artifacts that are particularly problematic (Fisher *et al.*, 2008). Various methods have been developed to tackle the problems caused by intra-fraction motion, e.g., real-time position management respiratory gating and synchronized moving aperture radiation therapy, most of them using embedded markers to track the position of the region of interest (ROI). Image guided radiotherapy treatment (IGRT) is another complementary approach aimed at tackling the problem of inter-fraction motion. This approach commonly uses a so-called cone-beam imaging (CBI) technique to acquire 3D volumetric data immediately prior to treatment delivery. Although much work has been published on the effect of organ motion and techniques compensating for it during radiotherapy treatment, the problems caused by shape variations in the tumor have been largely ignored. To address this problem, a method combining active shape models (ASM) and electronic portal imaging devices (EPID) to avoid markers was suggested by Su *et al.* (2007). The initial contour in the ASM is not set automatically but manually. Thus, the initialization for the ASM is time consuming. In addition, the registration with the EPID image may be prone to errors.

In this paper, we argue for 3D modeling of a set of ROIs by means of a geometrical and physics-based deformable model, that is, energy minimizing deformable models based on geodesic and finite element models (GAR-FEM model). Using the implemented GAR-FEM model to accurately track the clinical target volume, a full implementation of IGRT is possible using only the 2D CT data without markers. As well, it may be used for accurate segmentation in the clinical target planning (CTP), all this leading to adaptive radiotherapy. In this process, intra/inter-fraction tumour shape and position can be accurately detected and tracked; thus, the dose delivery for treatment fractions can also be adaptively modified to compensate for inaccuracies in dose delivery.

The 3D modeling is applied to prostate cancer ROIs, that is, bladder and rectum. Bladder and rectum are considered as the organs to be protected against high dose of radiation during treatment of prostate cancer (Costa *et al.*, 2007; Haas *et al.*, 2008; Banik *et al.*, 2009). The application of a both geodesic and physics-based model for 3D modeling of ROIs from a 2D CT image set of the pelvic area has not been considered before.

A number of papers dealing with bladder segmentation have been published in recent years; a good survey has been done by Shi *et al.* (2009). These methods are based on mathematical morphology (Bueno *et al.*, 2001; Camapum *et al.*, 2004), region growing (Bueno *et al.*, 2001; Mazonakis *et al.*, 2001; Haas *et al.*, 2008), shape deformation including geometric (Gibou *et al.*, 2005; Rousson *et al.*, 2005) and parametric models (Bueno *et al.*, 2004) constrained by means of simple mesh (Costa *et al.*, 2007), and atlas based (Ripoche *et al.*, 2004) initialization. All of these present their advantages against manual delineation, but still they have some drawbacks due to the large variations of bladder geometry between patients and the limited contrast between the bladder and nearby organs.

Previous works by the authors using mathematical morphology methods (Bueno *et al.*, 2001; Camapum *et al.*, 2004) have shown how difficult it is to prevent the extracted bladder contour from leaking into nearby ROIs due to non-contrast. They have also shown how parametric models are dependent on the initial control points without preserving topological changes within the ROIs (Bueno *et al.*, 2004). To overcome these limitations, in this study, we were interested in ROI segmentation using geometrical deformable models, which will also be used for tracking. Moreover, to accommodate and model the ROIs non-rigidly and the inter-patient anatomical differences, a physics-based model is considered. Deformable models offer a powerful approach to accommodating the significant variability of biological structures over time and across different individuals.

Thus, the purpose of our GAR-FEM model strategy is twofold, first to automatically detect and track the ROI and then to statistically parameterize and model the ROI variations and their spatial relationship. Geodesic models can handle topological changes as the surface evolves in time and it is insensitive to the initialization. FEM models have 3D point-to-point correspondence and they have short-term rotational and translational invariance. The next sections describe the methods applied and the results obtained. Finally, the conclusions of this study and future research directions are drawn.

2 Methods

Surface-interest modeling using active contours and deformable surfaces has become a field of renewed activity. Classical techniques for representing deformable models were developed by Terzopoulos and Fleischer (1988) and by Kass *et al.* (1988) providing the well-known snakes method. Since then, a wide range of computer graphics and image processing applications including medical applications have used energy minimizing deformable methods.

The mathematical foundations of deformable models represent the confluence of geometry, physics, and approximation theory. Geometry serves to represent object shape, physics imposes constraints on how the shape may vary over space and time, and optimal approximation theory provides the formal mechanisms for fitting the models to measured data. The physical interpretation views deformable models as elastic bodies which respond to applied force and constraints.

The next section contains a brief introduction to the mathematical foundations of deformable models. Then the geodesic model used to detect the ROI and obtain the ROI contour input to the FEM model is described. Section 2.3 describes the application of the physics-based statistical deformable model for 3D modeling of anatomical structures from a set of 2D image sequences applied to CTs of the the pelvic area.

2.1 Energy minimizing deformable models

The contour under a deformable model parameterization may be represented as a curve, $v(s) = (x(s), y(s))$, where x and y are the coordinate functions and $s \in [0, 1]$ is the parametric domain. The curve evolves until the ROI, subject to constraints from a given image, $I(x, y) : \mathcal{R} \to R$. Thus, initially a curve is set around the ROI that, via minimization of an energy functional, moves normal to itself and stops at the boundary of the ROI (Kass *et al.*, 1988). The energy functional is defined as

$$E_c(s) = \int_0^1 \Big[E_{\text{int}}(v(s)) + E_{\text{ext\_pot}}(v(s))\Big] \mathrm{d}s. \quad (1)$$

The first term, E_{int}, represents the internal energy of the spline curve due to mechanical properties of the contour, stretching and bending (Kass *et al.*, 1988). It is a sum of two components, the elasticity and rigidity energy:

$$E_{\text{int}}(v(s)) = \left(\frac{\alpha(s)}{2}\left|v_s(s)\right|^2 + \frac{\beta(s)}{2}\left|v_{ss}(s)\right|^2\right), \quad (2)$$

where $\alpha(s)$ controls the tension of the contour, while $\beta(s)$ controls its rigidity. Thus, these functions determine how the contour can stretch or bend at any point s of the spline curve.

The second term couples the contour to the image:

$$E_{\text{ext\_pot}}(v(s)) = P(v(s)) = -c\left|\nabla[G_\sigma * I(x, y)]\right|, \quad (3)$$

where $P(v(s))$ denotes a scalar potential function defined on the image plane. It is responsible for attracting the contour towards the object in the image (external energy). Therefore, it can be expressed as a weighted combination of energy functionals. To apply this contour parameterization to images, external potentials are designed such that local minima coincide with intensity extrema, edges, and other image features of interest. For example, the contour will be attracted to intensity edges in an image by choosing a potential equal to the gradient; see Eq. (3) where c scales the magnitude of the potential and $G_\sigma * I(x, y)$ denotes the image convolved with a Gaussian smoothing filter.

The problem now is how to solve Eq. (1) to avoid sensitivity to the initial contours and to handle changes in shape topology. Some techniques have been proposed to solve Eq. (1) (Bueno, 2008). These techniques are based on information fusion, dealing with active contour models in addition to region properties and curvature driven flows. The latest are the ones adopted in our research, as described in the following section.

2.2 Geodesic active contour and region model

Recently, there has been an increasing interest in level set methods for different applications (Osher and Paragios, 2003; Lee *et al.*, 2008). Here, we follow the methods of Malladi *et al.* (1995) and Caselles *et al.* (1997) in the context of shape detection. The approach is motivated by the snake approach given by Kass *et al.* (1988).

Let us consider a particular class of contour models in which the rigidity coefficient is set to zero, that is $\beta = 0$. This will allow achieving smooth curves in the proposed approach without having the

high-order smoothness given by $\beta \neq 0$ in energy-based approaches. Moreover, this smoothness component in Eq. (1) appears in order to minimize the total squared curvature. It is possible to prove that the curvature flow decreases the total curvature. The use of the curvature-driven curve motions as smoothing terms proved to be very efficient in previous research (Malladi *et al.*, 1995; Caselles *et al.*, 1997). Therefore, curve smoothing will also be obtained with $\beta = 0$, having only the first regularization term in Eq. (1) and $P(v(s)) = -c\,|\nabla I[v(s)]|$.

It is possible to extend the level set space and introduce prior knowledge about the expected intensity properties of the ROI, and thus account for boundary and global region-driven information (Paragios, 2002). To this end, the input image is partitioned into two non-overlapping regions; that is, $\mathcal{P}(\mathcal{R}) = (\mathcal{R}_{\mathcal{A}}, \mathcal{R}_{\mathcal{B}})$, where $\mathcal{R}_{\mathcal{A}}$ is the ROI and $\mathcal{R}_{\mathcal{B}}$ the background, with conditional density functions defined by $p_{\mathcal{A}}(I)$ and $p_{\mathcal{B}}(I)$. The boundaries of the ROI are denoted by $\partial\mathcal{R}_{\mathcal{A}}(s)$ and by $p(\partial\mathcal{R}_{\mathcal{A}}|\mathcal{B})$ the conditional boundary density function that measures the probability of a given point being at the real boundary of $\mathcal{R}_{\mathcal{A}}$. Then, the ROI can be obtained using the geodesic active contour framework, thus minimizing the following equation:

$$E(\partial\mathcal{R}_{\mathcal{A}}) = \alpha \underbrace{\int_0^1 |\partial\dot{\mathcal{R}}_{\mathcal{A}}|^2 \mathrm{d}s}_{\text{Internal term}} + (1-\alpha) \underbrace{\int_0^1 g(s)p(\partial\mathcal{R}_{\mathcal{A}}|\mathcal{B})\mathrm{d}s}_{\text{External term}}, \tag{4}$$

where $\alpha \in [0,1]$ is a constant balancing the contribution of the two terms, and $g(s)$ is a strictly decreasing function working as a stopping function. The maximization of the a posteriori probability function is equivalent to the minimization of the $[-\lg()]$ function of this probability. Then, applying Bayes' rule Eq. (4) may be generalized as follows:

$$\begin{aligned} E(\partial\mathcal{R}_{\mathcal{A}}) = \; & \alpha \underbrace{\int_0^1 \overbrace{g(s)p(\partial\mathcal{R}_{\mathcal{A}}(s))}^{\text{Boundary attraction}} \; |\partial\dot{\mathcal{R}}_{\mathcal{A}}|\mathrm{d}s}_{\text{Contour term}} \\ & -(1-\alpha)\overbrace{\Big[\int\int_{\mathcal{R}_{\mathcal{A}}} \lg(p_{\mathcal{A}}(I))\mathrm{d}x\mathrm{d}y}^{\text{Contour term}} \\ & + \underbrace{\int\int_{\mathcal{R}_{\mathcal{B}}} \lg(p_{\mathcal{A}}(I))\mathrm{d}x\mathrm{d}y\Big]}_{\text{Region term}}. \end{aligned} \tag{5}$$

The minimization of Eq. (5) is performed using a gradient descent method, defining an embedding function of the curve $v(s)$, $\psi(t,s)$. That is an implicit representation of $v(s)$; assuming that $v(s)$ is a level set of a function $\psi(t,s) : [0,a] \times [0,b] \to \mathcal{R}$, the following partial differential equation (PDE) for curve and surface evolution is derived:

$$\begin{aligned} \frac{\partial\psi}{\partial t} &= \alpha \lg\left(\frac{p_{\mathcal{B}}(I)}{p_{\mathcal{A}}(I)}\right)|\nabla\psi| \\ &\quad + (1-\alpha)\left(g(s)\mathcal{K}\,|\nabla\psi| + \nabla\psi\nabla g\right), \end{aligned} \tag{6}$$

where $\mathcal{K}$ is the Euclidean curvature in the direction of the normal $\boldsymbol{N}$ and the stopping function used $g(s)$ is defined by $g(s) = 1/(1+|\nabla G_\sigma * I(x,y)|)$.

The probability functions are obtained by means of a statistical analysis based on the image histogram. The model studies the histogram of the region inside the contour, obtaining the standard deviation, σ, and the mean intensity, μ. By using these measures the probability distribution function is obtained based on the square error between each pixel intensity and the distance to the ROI. Thus the region term is defined as

$$\alpha \sum_{I(x,y)\in\mathcal{R}_{\mathcal{A}}} \sqrt{[(\mu+\sigma) - I(x,y)]^2 + [(\mu-\sigma) - I(x,y)]^2}. \tag{7}$$

The motion PDE obtained has two forces acting on the curve, both in the direction of $\boldsymbol{N}$: (1) the region force that tries to shrink or to expand the curve in the direction that maximizes the information provided by this partition ($\mathcal{R}_{\mathcal{A}}$) and (2) the contour force. The contour force contains two subterms, one that moves the curve toward the region boundaries by the curvature effect and the other that stops the curve.

As previously mentioned, the advantage of using this model is that the algorithm can handle changes in the topology of the shape as the surface evolves in time, and it is less sensitive to the initialization. This may be seen in Fig. 1, where the geodesic active contour and region (GAR) model is illustrated on the Shepp-Logan phantom image (Shepp and Logan, 1974) and compared to the geometrical (Malladi *et al.*, 1995) and geodesic (Caselles *et al.*, 1997) level set methods. These methods follow the motion PDEs shown in Eqs. (8) and (9), respectively:

$$\frac{\partial\psi}{\partial t} = g(s)\left(\nu + \mathcal{K}\right)|\nabla\psi|, \tag{8}$$

$$\frac{\partial \psi}{\partial t} = g(s)\left(\nu + \mathcal{K}\right)|\nabla \psi| + \nabla \psi \nabla g, \tag{9}$$

where ν is a real constant of speed called balloon force.

The objective in Fig. 1 is to segment the ROI with topological changes starting with a random initialization in the middle of the image (Fig. 1a). After several iterations of the contour (20 iterations in Fig. 1b and 50 iterations in Fig. 1c), the final result is shown in Fig. 1d, where the ROI has been properly segmented. It must be said that the level set methods are strongly affected by the choice of parameters, mainly the speed and the standard deviation of the Gaussian. The comparison in Fig. 1 was made for the same parameters: standard deviation of the Gaussian $\sigma = 1.0$, $\nu = 0.31$ and for the GAR model $\alpha = 0.25$.

The GAR method is less sensitive to noise and may be used in real time for 4D sequences, that is for tracking. The use of the GAR model in real time for tracking is shown in Fig. 2, where the method is applied every five frames to a video sequence of the heart. The parameters used were the same as previously mentioned, since they provided the best results. Further results provided by the authors may be seen from http://www.maestro-research.org/imaging.htm for lung video sequences. Fig. 2 also shows how the method works properly with complex shapes, such as the heart.

Some results of the GAR model for the application of interest are shown in Fig. 3 with the tracking of the bladder and rectum in a 2D set of pelvic CT images. In order to assess the performance of the segmentation, the results were compared against those obtained by manual segmentation, and quantitative measures including sensitivity and specificity were obtained. Fig. 4 illustrates this validation with some examples of the pelvic CT images considered. The results of manual delineation (Fig. 4a) are compared against the segmentation (Fig. 4b) and the contours extracted are superimposed in Fig. 4c for qualitative validation. The average values of sensitivity and specificity defined in terms of the number of true positives (TP), true negatives (TN), false positives (FP), and false negatives (FN) detections (Eq. (10), Bueno *et al.*, 2001; Déniz *et al.*, 2010) were 93.3% and 99.2% respectively. The worst values for the sensitivity and specificity were 87.2% and 98.3% respectively. In this case,

$$\text{sensitivity} = \frac{\text{TP}}{\text{TP} + \text{FN}}, \quad \text{specificity} = \frac{\text{TN}}{\text{TN} + \text{FP}}. \tag{10}$$

The GAR model works properly with any initialization and preserving the topology; however, it may have some problems when the ROI presents high standard deviation of intensities. This problem can be seen in the case of the heart in Fig. 5. This figure is a zoom of the 3rd frame in Fig. 2, where the two regions in which the GAR has been divided are shown. That is, the heart is just one ROI with a large contrast and the GAR model assumes two ROIs. This may also occur in the CT images of the pelvic area when the bladder is partially filled. This problem may be solved with the 3D modeling of the ROI by means of the FEM model, and then initializing the tracking with it. This model is explained in the next section.

2.3 Statistical physics-based deformable model

Once the different organs are segmented they are modeled by means of a statistical physics-based deformable model. The proposed approach was motivated by the technique presented in a previous work by the authors (Nikou *et al.*, 2001) based on Nastar and Ayache (1996) and Pentland and Sclaroff (1991). The proposed method has been extended, however, to parallel processing, since the dimension of CT images is very large, and it is applied to a sequence of 2D CT images instead of 3D magnetic resonance images (MRI). Thus, the 2D axial images have been previously projected and interpolated to generate the transversal and sagittal views to apply the model on the 3D data sequences.

A vector containing the vibration modes of each ROI is then associated to each 3D segmented organ. The most significant variation modes of a Karhunen-Loeve (KL) transformation applied to the same organ parameterize this vector. The model consists of a set of 3D discrete points located on a surface with cylinder topology. Thus, the vector nodes are stacked in the following vector:

$$\boldsymbol{X}_0 = [x_1^0, y_1^0, z_1^0, ..., x_{N'N}^0, y_{N'N}^0, z_{N'N}^0]^{\mathrm{T}}, \tag{11}$$

where $\boldsymbol{X}_0$ is the initial mesh, N is the number of points in the X axis, and N' is the number of points in the Y axis.

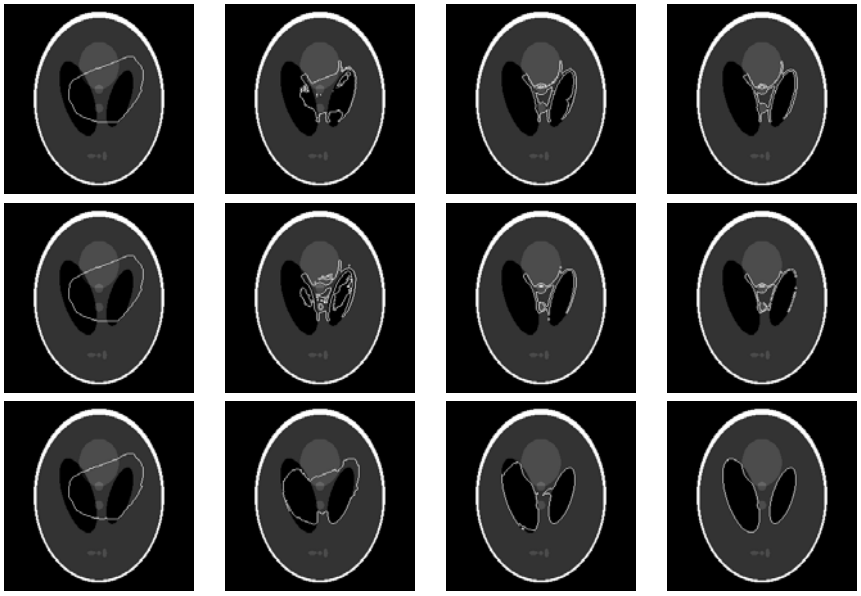

(a) (b) (c) (d)

Fig. 1 Segmentation applied to a phantom. 1st row: results of the geometric or snake model; 2nd row: results of the level set model; 3rd row: results of the geodesic active contour and region (GAR) model. (a) Initial contour; (b) 20 iterations; (c) 50 iterations; (d) Final detection

Thus, the contour is represented by a closed mesh of $i = NN'$ virtual nodes with mass m_i, linked between them by virtual springs. These mass-spring elements have stiffness forces, $\boldsymbol{f}_{\mathrm{s}i}$, dumping ones, $\boldsymbol{f}_{\mathrm{d}i}$, and external attracting forces between the nodes and the exact contour of the image, $\boldsymbol{f}_{\mathrm{i}i}$. Then, the equilibrium of these forces on a node, i, may be parameterized by the following equation:

$$m_i\ddot{\boldsymbol{r}}_i = \boldsymbol{f}_{\mathrm{s}i} + \boldsymbol{f}_{\mathrm{d}i} + \boldsymbol{f}_{\mathrm{i}i}, \tag{12}$$

where $\boldsymbol{r}_i$ is the position vector of point i. It is supposed that the natural elongation of the virtual mass-spring elements is null. The mass-spring element between neighbor points i, j has a stiffness constant k_{ij} and, therefore, the elastic forces on each node are given by the following equation:

$$\boldsymbol{f}_{\mathrm{s}i} = -k_{(i-1)(i)}\boldsymbol{r}_{(i-1)(i)} + k_{(i)(i+1)}\boldsymbol{r}_{(i)(i+1)}. \tag{13}$$

The dumping forces on the nodes are those proportional to the global speed and those proportional to the relative speed of neighbor nodes. Thus $\boldsymbol{f}_{\mathrm{d}i}$ is given by

$$\boldsymbol{f}_{\mathrm{d}i} = -c_i\ddot{\boldsymbol{r}}_i - c_{(i-1)(i)}\ddot{\boldsymbol{r}}_{(i-1)(i)} + c_{(i)(i+1)}\ddot{\boldsymbol{r}}_{(i)(i+1)}. \tag{14}$$

$\boldsymbol{f}_{\mathrm{i}i}$ is considered as the Hausdorff distance between the mesh nodes and the nearest points belonging to the segmented contour.

The set of dynamic equations for all the mesh nodes may be written as a set of second-order ordinary differential equations for the displacement of $\boldsymbol{X}_0(t)$, that is $\boldsymbol{U}(t)$:

$$\boldsymbol{M}\ddot{\boldsymbol{U}} + \boldsymbol{C}\dot{\boldsymbol{U}} + \boldsymbol{K}\boldsymbol{U} = \boldsymbol{F}, \tag{15}$$

where $\boldsymbol{M}$ is a diagonal matrix corresponding to the mass nodes, $\boldsymbol{K}$ is the three-diagonal stiffness matrix, $\boldsymbol{C}$ corresponds to the dumping matrix, and $\boldsymbol{F} = \boldsymbol{f}_{\mathrm{i}i}$ is the external force. Eq. (15) is solved in the equilibrium state; that is, it corresponds to the static problem $\boldsymbol{K}\boldsymbol{U} = \boldsymbol{F}$. Moreover, this equation is solved in a subspace corresponding to the truncated vibration modes of the deformable structure. More details regarding all the adopted assumptions are presented in Nikou *et al.* (2001).

The number of vibration modes retained in the object description is chosen to obtain a compact, but adequately accurate, representation. A typical a priori value covering many types of standard deformations is the quarter of the number of degrees of freedom in the system (i.e., 25% of the modes are kept). Although not providing a high resolution

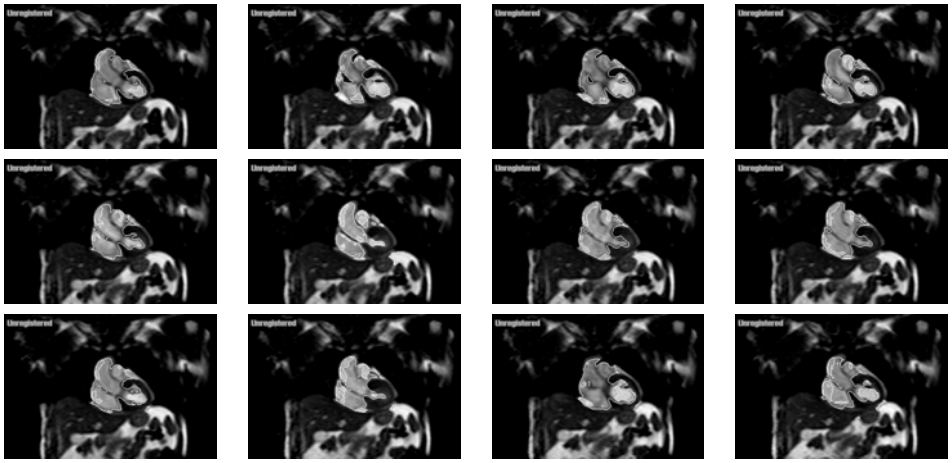

Fig. 2 Geodesic active contour and region (GAR) model tracking applied to a video sequence of the heart

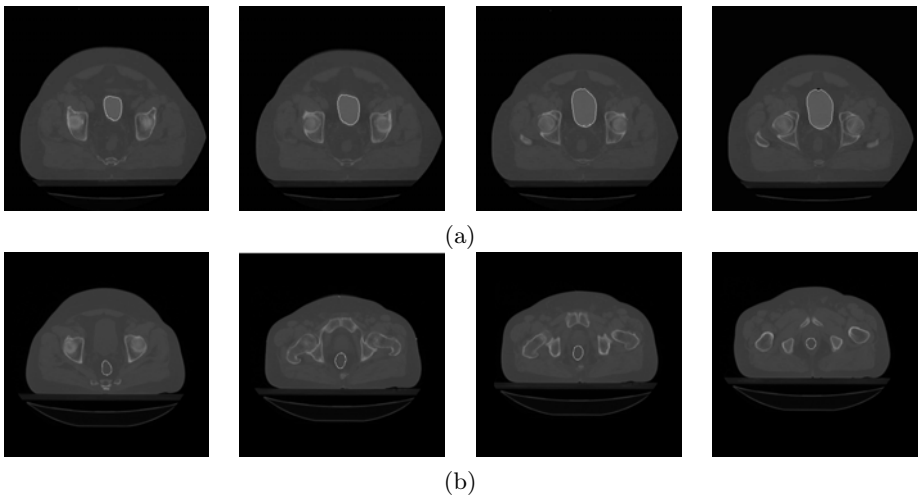

Fig. 3 Geodesic active contour and region (GAR) model segmentation applied to ROIs in CT images of the pelvic area for radiotherapy treatment planning (RTP). (a) Bladder segmentation; (b) Rectum segmentation

description of the surfaces, this truncated representation provides a satisfactory compromise between accuracy and complexity of the representation. The mesh model is initialized around the structures of interest and the vibration amplitudes are then explicitly computed.

Thus, the surfaces of each anatomical structure are parameterized by the amplitudes of the vibration modes of a deformable mesh with cylinder topology. For a given image in the training set, a vector containing the largest vibration modes describing the different deformable surfaces is created. This random vector is statistically constrained by retaining the most significant variation modes of its KL expansion on the training population. By these means, the conjunction of surfaces is deformed according to the anatomical variability observed in the training set. The statistically learned deformable model represents the relative location of different anatomical surfaces and it is able to accommodate their significant variability across different individuals. Furthermore, as previously mentioned, the advantage of using the FEM model is that they are invariant to small rotations and translations; that is, in those cases there is no need to register the segmented ROIs.

The following pseudocode gives a global vision of the deformable model processing structure:

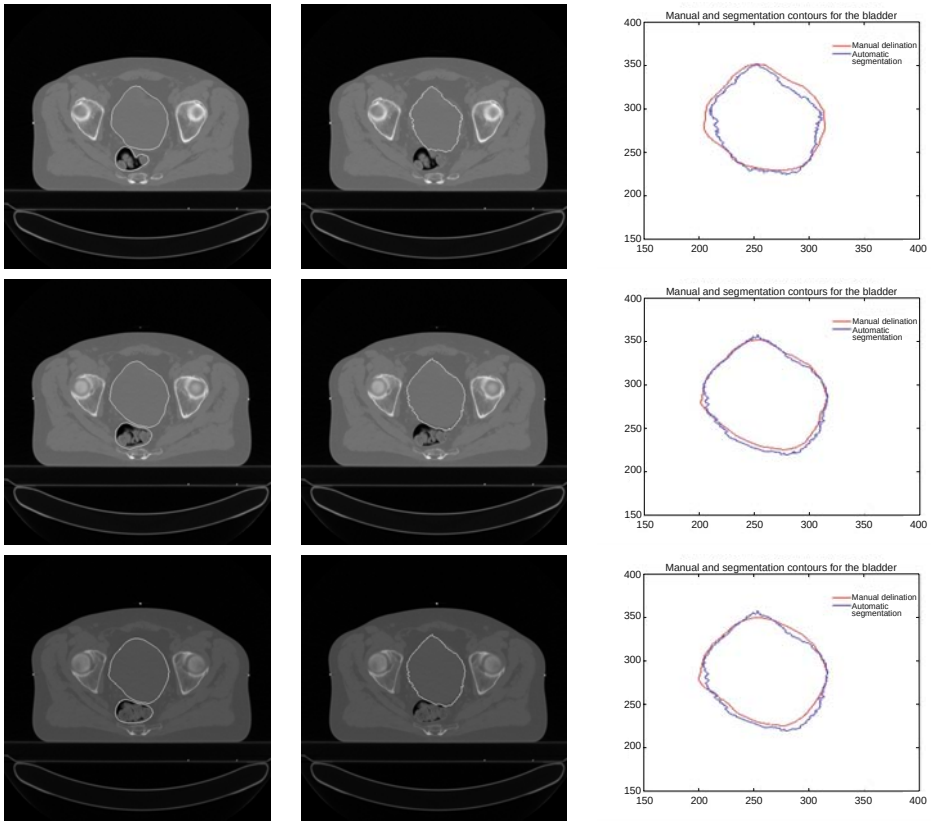

(a) (b) (c)

Fig. 4 Quantitative validation. (a) Manual delineation; (b) Automatic segmentation; (c) Contour comparison

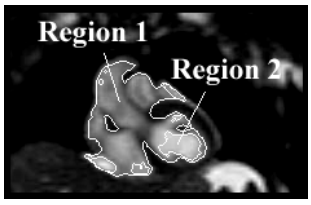

Fig. 5 Zoom of the 3rd frame from the video sequence of the heart in Fig. 2

```
WHILE i<NumberOfPatients
    WHILE j<NumberOfROIs
        SegmentROI;
        DeformMesh;
        SaveAmplitudes;
    END WHILE j
END WHILE i

WHILE i<NumberOfROIs
    WHILE j<NumberOfPatients
    %Using saved amplitudes
        Generate3DGlobalModel;
    END WHILE j
END WHILE i

WHILE j<NumberOfROIs
    CombineDifferentROIs;
END WHILE j
```

3 Results

In this section, the results corresponding to the 3D modeling process are shown. The first step consists of the selection of a representative dataset. A representative dataset including different anatomical structures of interest is used to initialize the deformable model. Datasets are provided by Grupo IMO (Instituto Madrileño de Oncología) and consist of 2D CT image sequences for the pelvic zone.

To improve the model accuracy, it is important to use a large number of data volumes. Nine CTs ($512 \times 512 \times 30$) volumes were used as the test

datasets at the present research results. The number of CTs, however, is continuously increased to obtain a more accurate representation of the ROIs.

As mentioned in Section 2.3, once each organ or ROI is segmented using the geodesic active model, they are modeled using the physics-based model. The ROIs are initialized using an initial mesh with cylinder topology and defined by a set of points using X, Y coordinates. Generally speaking 50×40 points are enough for the ROIs in the pelvic region. These ROIs, for the application of interest within this work, are the bladder and rectum. Figs. 3 and 4 show the results of the geodesic active model applied to these regions on several 2D CT sequences of the human pelvic area. Fig. 6a shows one set of the original 2D CT image sequences considered. Fig. 6b shows the initial mesh containing the segmented ROIs bladder and rectum of the image sequence.

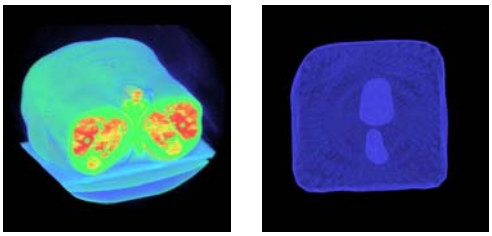

(a) (b)

Fig. 6 Original 2D CT image sequence and the modeling mesh with the segmented organs. (a) Original sequence; (b) Modeling and deformed mesh

The quadratic sphere is progressively deformed to obtain a representative set of amplitudes. The initial mesh is shown after some deformations. The resulting amplitudes represent the deformations applied to the mesh surface to be adapted to the exact contour of the ROI by means of its vibration modes. Each region was parameterized by 2000 points (50×40) and keeping 500 vibration modes (25% over the total number of points). The model obtains an accurate representation of the different ROIs. Fig. 7c shows the global modeled volume with both ROIs. The physics-based model may be applied to each ROI individually as illustrated in Figs. 7a and 7b for the bladder and rectum, respectively. Better accuracy levels can be obtained by increasing the number of vibration modes. The computational time to generate the parallel FEM model for the ROI and data taken into consideration ($2 \times 9 \times 512 \times 512 \times 30$) is about 20 min. The specific massive parallel processors (MPP) hardware solution used is composed by 17 nodes (Intel XEON with 3.2 GHz and 2 GB of RAM) with one independent processor per node. The dependencies between nodes and the communication have been analyzed using an INFINIBAND network with a bandwidth of 10 GB full duplex.

Once each structure has been independently modeled, a 3D global model including the whole set of ROIs is provided in terms of amplitude combination. The 3D global model for the pelvic area (rectum and bladder) can be seen in Fig. 7b as previously mentioned. The model can be adapted to new volumes that do not belong to the initial dataset. Thus, deformations are applied to the global model in order to adapt the model to new study cases improving the RTP. Figs. 8b–8d show some deformation results superimposed onto the original data at different views, the axial, sagittal, and transversal, compared against manual segmentation (Fig. 8a). Quantitative measures of sensitivity and specificity were also obtained for the 3D global model. The average values were improved by 1.2% and 0.3% for sensitivity and specificity respectively; that is, 94.5% was obtained for the sensitivity and 99.5% for the specificity. These results are due to the smooth surfaces provided using the FEM model.

4 Conclusions and future work

Overcoming technological advances related to the study of new oncologic therapies must be accompanied by a parallel development of tools that improve the precision in the detection, tracking, and modeling of ROIs. The objective is to optimize the conformation of the dose delivered to the target (tumoral tissues) whatever its shape in order to spare the surrounding tissues. In this context, simulation and anatomical variations modeling are a priority in radiotherapy treatment planning.

This work describes a generic and optimal model to track and model a set of ROIs, with independence of shape, from images of different modalities. Quantitative validations of the segmented and modeled ROIs have been done obtaining an average of 93.9% and 99.3% for the sensitivity and specificity, respectively.

Using the implemented model an image guided radiotherapy treatment is possible using only 2D CT

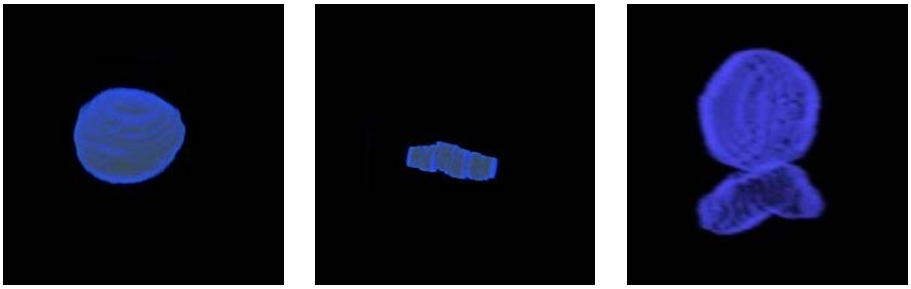

(a) (b) (c)

Fig. 7 Modeled regions of interest. (a) Modeled bladder; (b) Modeled rectum; (c) Global model

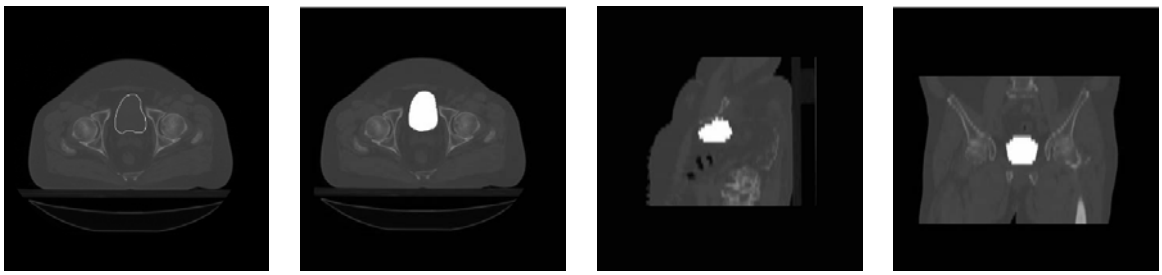

(a) (b) (c) (d)

Fig. 8 Manual and model segmentation. (a) Manual delineation; (b) Axial view; (c) Sagittal view; (d) Transversal view

data without markers. It remains as future work to apply the modeled structures in dosimetry studies and image registration (Bueno *et al.*, 2009), in order to integrate and validate them in the whole radiotherapy treatment context and in vivo dosimetry.

References

Banik, S., Rangayyan, R., Boag, G., 2009. Landmarking and Segmentation of 3D CT Images. Springer Berlin Heidelberg. [doi:10.1007/s11548-009-0289-y]

Bueno, G., 2008. Fuzzy Systems and Deformable Models. *In*: Haas, O.C.L., Burnham, K.J. (Eds.), Intelligent and Adaptive Systems in Medicine, Chapter 10. Series in Medical Physics and Biomedical Engineering. Taylor & Francis Group, London, p.305-329.

Bueno, G., Fisher, M., Burnham, K., 2001. Automatic Segmentation of Clinical Structures for RTP: Evaluation of a Morphological Approach. Proc. Medical Image Understanding and Analysis, p.73-76.

Bueno, G., Martínez, A., Adán, A., 2004. Fuzzy snake segmentation of anatomical structures applied to CT images. *LNCS*, **3212**:33-42.

Bueno, G., Déniz, O., Carrascosa, C., Delgado, J., Brualla, L., 2009. Fast Monte Carlo simulation on a voxelized human phantom deformed to a patient. *Med. Phys.*, **36**(11):5162-5174. [doi:10.1118/1.3245877]

Camapum, J., Silva, A., Freitas, A., Bassani, H., 2004. Segmentation of Clinical Structures from Images of the Human Pelvic Area. Proc. 17th Brazilian Symp. on Computer Graphics and Image Processing, p.10-16. [doi:10.1109/SIBGRA.2004.1352937]

Caselles, V., Kimmel, R., Sapiro, G., 1997. Geodesic active contours. *Int. J. Comput. Vis.*, **22**(1):61-79. [doi:10.1023/A:1007979827043]

Collier, D., Burnett, S., Amin, M., 2003. Assessment of consistency in contouring of normal-tissue anatomic structures. *J. Appl. Clin. Med. Phys.*, **4**(1):17-24. [doi:10.1120/1.1521271]

Costa, M., Delingette, H., Ayache, N., 2007. Automatic Segmentation of the Bladder Using Deformable Models. 4th IEEE Int. Symp on Biomedical Imaging: from Nano to Macro, p.904-907. [doi:10.1109/ISBI.2007.356999]

Déniz, O., Castrillón, M., Lorenzo, J., Antón, L., Hernandez, M., Bueno, G., 2010. Computer vision based eyewear selector. *J. Zhejiang Univ.-Sci. C (Comput. & Eletron.)*, **11**(2):79-91. [doi:10.1631/jzus.C0910377]

Fisher, M., Su, Y., Aldridge, R., 2008. Some Applications of Intelligent Systems in Cancer Treatment: a Review. *In*: Haas, O.C.L., Burnham,

K.J. (Eds.), Intelligent and Adaptive Systems in Medicine, Chapter 9. Series in Medical Physics and Biomedical Engineering. Taylor & Francis Group, London, p.283-303.

Foskey, M., Davis, B., Goyal, L., Chang, S., Chaney, E., Strehl, N., Tomei, S., Rosenman, J., Joshi, S., 2005. Large deformation three-dimensional image registration in image-guided radiation therapy. *Phys. Med. Biol.*, **50**(24):5869-5892. [doi:10.1088/0031-9155/50/24/008]

Gibou, F., Levy, D., Cádenas, C., 2005. Partial differential equations based segmentation for radiotherapy treatment planning. *Math. Biosci. Eng.*, **2**(2):209-226.

Haas, B., Coradi, T., Scholz, M., Kunz, P., Huber, M., Oppitz, U., André, L., Lengkeek, V., Huyskens, D., van Esch, A., *et al.*, 2008. Assessment of consistency in contouring of normal-tissue anatomic structures. *Phys. Med. Biol.*, **53**(6):1751-1771. [doi:10.1088/0031-9155/53/6/017]

Kass, M., Witkin, A., Terzopoulos, D., 1988. Snakes: active contour models. *Int. J. Comput. Vis.*, **1**(4):321-331. [doi:10.1007/BF00133570]

Lee, C., Chung, P., 2004. Identifying Abdominal Organs Using Robust Fuzzy Inference Model. IEEE Int. Conf. on Networking, Sensing and Control, **2**:1289-1294. [doi:10.1109/ICNSC.2004.1297133]

Lee, M., Park, S., Cho, W., Kim, S., Jeong, C., 2008. Segmentation of medical images using a geometric deformable model and its visualization. *Can. J. Electr. Comput. Eng.*, **33**(1):15-19. [doi:10.1109/CJECE.2008.4621790]

Malladi, R., Sethian, J., Vemuri, B., 1995. Shape modeling with front propagation: a level set approach. *IEEE Trans. PAMI*, **17**(4):158-175.

Mazonakis, M., Damilakis, J., Varveris, H., Prassopoulos, P., Gourtsoyiannis, N., 2001. Image segmentation in treatment planning for prostate cancer using the region growing technique. *Br. J. Radiol.*, **74**:243-249.

Nastar, C., Ayache, N., 1996. Frequency-based nonrigid motion analysis. *IEEE Trans. PAMI*, **18**(11):1069-1079. [doi:10.1109/34.544076]

Nikou, C., Bueno, G., Heitz, F., Armspach, J., 2001. A joint physics-based statistical deformable model for multimodal brain image analysis. *IEEE Trans. Med. Imag.*, **20**(10):1026-1037. [doi:10.1109/42.959300]

Osher, S., Paragios, N., 2003. Geometric Level Set Methods in Imaging, Vision and Graphics. Springer-Verlag New York.

Paragios, N., 2002. A level set approach for shape driven segmentation and tracking of the left ventricle. *IEEE Trans. Nucl. Sci.*, **21**(3):21-43.

Pentland, A., Sclaroff, S., 1991. A closed-form solutions for physically-based shape modelling and recognition. *IEEE Trans. PAMI*, **13**(7):730-742.

Ripoche, X., Atif, J., Osorio, A., 2004. A 3D Discrete Deformable Model Guided by Mutual Information for Medical Image Segmentation. Proc. Medical Imaging Conf., p.1-3.

Rousson, M., Khamene, A., Diallo, M., 2005. Constrained surface evolutions for prostate and bladder segmentation in CT images. *LNCS*, **3765**:251-260. [doi:10.1007/11569541_26]

Shepp, L., Logan, B., 1974. The Fourier reconstruction of a head section. *IEEE Trans. Med. Imag.*, **22**(6):773-776.

Shi, F., Yang, J., Zhu, Y., 2009. Automatic segmentation of bladder in CT images. *J. Zhejiang Univ.-Sci. A*, **10**(2):239-246. [doi:10.1631/jzus.A0820157]

Su, Y., Fisher, M., Rowland, R.S., 2007. Markerless intra-fraction organ motion tracking using hybrid ASM. *Int. J. Comput. Assist. Radiol. Surg.*, **2**(3-4):231-243. [doi:10.1007/s11548-007-0133-1]

Terzopoulos, D., Fleischer, K., 1988. Deformable models. *The Vis. Comput.*, **4**(6):306-331. [doi:10.1007/BF01908877]

Webb, S., 2006. Does elastic tissue intrafraction motion with density changes forbid motion-compensated radiotherapy? *Phys. Med. Biol.*, **51**(6):1449-1462. [doi:10.1088/0031-9155/51/6/006]